Contents list available at CBIORE journal website

International Journal of Renewable Energy Development

Journal homepage: https://ijred.cbiore.id

Research Article

Hybrid precursor engineering of g-C_3N_4 toward improved α-Fe_2O_3/g-C_3N_4 photoanodes under HMF hole-scavenging conditions

Muhammad Ibadurrohman[1,2,*], Regina Ulibasa[1], Nadia Mumtazah[1], Nurfadlih Syahlani[3]

[1]*Department of Chemical Engineering, Faculty of Engineering, Universitas Indonesia, Depok, West Java 16424, Indonesia*

[2]*Tropical Renewable Energy Center, Faculty of Engineering, Universitas Indonesia, Kampus UI Depok16424, Indonesia*

[3]*Research Center for Testing Technology and Standards, National Research and Innovation Agency, PUSPIPTEK Area, Tangerang Selatan, Banten 15314, Indonesia*

Abstract. The sluggish kinetics of Oxygen Evolution Reaction (OER) is a challenge for the development of efficient photoelectrochemical (PEC) systems for sustainable hydrogen production. In this work, α-Fe_2O_3/g-C_3N_4 photoanodes were prepared from g-C_3N_4 of different precursors (urea, melamine and/or dicyandiamide) to investigate the influence of hybrid precursor engineering on the photoelectrochemical properties of the heterostructures. The incorporation of hybrid precursor derived g-C_3N_4 modified the structural and optical properties of the composite photoanodes and resulted in enhanced PEC response compared to single precursor systems. The as prepared composite with g-C_3N_4 prepared from ternary hybrid precursors (urea, melamine and dicyandiamide) showed the best performance among the as prepared samples with lowest onset potential (0.01 V) and highest ΔE (0.88 V) under the present experimental conditions. Photoluminescence analysis indicated a lower emission intensity of the ternary hybrid precursor-derived sample, which was attributed to the inhibited charge carriers recombination. Furthermore, the addition of 5-hydroxymethylfurfural (HMF) as a model organic substrate increased the photocurrent density (~95%) with no change in the onset potential, demonstrating the effective hole scavenging ability of the HMF. Chronopotentiometry measurements confirmed stable operation during continuous illumination. These findings demonstrate that the hybrid precursor engineering of g-C_3N_4 can affect the PEC behavior of α-Fe_2O_3/g-C_3N_4 photoanodes under HMF-assisted conditions.

Keywords: α-Fe_2O_3 photoanode; g-C_3N_4 heterojunction; Hybrid precursor engineering; 5-hydroxymethylfurfural oxidation; Charge separation

Received: 5th May 2026; Revised: 18th June 2026; Accepted: 27th July 2026; Available online: 16th August 2026

1. Introduction

Hydrogen has become a promising clean energy carrier for its high energy density (Møller *et al.*, 2017) and environmentally benign combustion product (Hossain Bhuiyan & Siddique, 2025). It is both a fuel for fuel cell technologies and an important feedstock for the chemical industry, especially for ammonia (AlZohbi, 2025; Bzovsky & Kudriavtsev, 2025), methanol (Hren *et al.*, 2024), and other value-added (Hren *et al.*, 2023) chemicals. But today, most hydrogen is still produced via steam methane reforming (Szablowski *et al.*, 2025), a process using fossil resources and producing huge amounts of CO_2 emissions, known as "gray hydrogen"(Dumančić *et al.*, 2024). These environmental concerns have led to significant interest in sustainable hydrogen production methods, such as water electrolysis powered by renewable energy (Al Dhahri *et al.*, 2026). Photoelectrochemical (PEC) water splitting is presented as a promising method for sustainable hydrogen production through the direct conversion of solar energy to chemical energy (Kamat & Sivula, 2022). In contrast to conventional electrolysis, PEC systems exploit the properties of semiconductor materials to absorb photons and produce electron-hole pairs, which trigger redox reactions at the electrode surface. In this process, the semiconductor is directly involved in the conversion of light energy into electrical charges, where an internal electric field assists the separation of photogenerated electrons and holes (van de Krol, 2012). The semiconductor properties such as band gap, stability, cost, and photocurrent response are greatly affected by the efficiency of PEC systems (Zhu *et al.*, 2022). However, the oxygen evolution reaction (OER) at the photoanode is one of the main limitations in PEC water splitting because it demands high energy due to its sluggish kinetics, even though oxygen has a limited economic value (Corbin *et al.*, 2024). Several strategies have been developed to improve PEC efficiency in overcoming this limitation, which are based on reducing energy consumption and improving reaction kinetics (Chiang *et al.*, 2012). One promising approach is to replace the OER with alternative oxidation reactions that are thermodynamically more favorable, such as the oxidation of biomass-derived molecules, such as 5-hydroxymethylfurfural (HMF) (Luo *et al.*, 2021; Mumtazah *et al.*, 2026).

HMF is an important platform chemical derived from biomass, obtained through the conversion of simple sugars such as fructose and glucose. It is a precursor to an array of high value chemicals such as fuels, polymers and chemical intermediates

* Corresponding author
Email: ibad@che.ui.ac.id (M. Ibadurrohman)

https://doi.org/10.61435/ijred.2026.62699
ISSN: 2252-4940/© 2026.The Author(s). Published by CBIORE

(Arabi *et al.*, 2026; Zhang *et al.*, 2020). The use of HMF as an alternative oxidation substrate in PEC systems has advantages over water oxidation in terms of a lower overpotential and improved reaction thermodynamics (Luo *et al.*, 2021). Therefore, HMF-assisted PEC systems may improve charge utilization at the photoanode by facilitating hole consumption and suppressing competing OER pathways. The oxidation of HMF has been reported to be thermodynamically more favorable than OER.OER has a ΔG° of 237.2 kJ/mol and a redox potential of 1.23 V. The oxidation of HMF to 2,5-diformylfuran (DFF), however, has a much lower ΔG° of 178 kJ/mole (Ayed *et al.*, 2020; Liu *et al.*, 2021). Furthermore, DFF is a high value chemical with a market value far higher than that of HMF (Dubbink *et al.*, 2021). These advantages suggest that the replacement of OER with HMF-assisted oxidation processes may improve PEC performance while potentially enabling simultaneous value-added chemical conversion.

α-Fe_2O_3 (hematite) is one of the most studied semiconductor materials for PEC systems because of its abundance, low cost, non-toxicity and suitable band gap (~2.20 eV) (Zeng *et al.*, 2015). However, its performance is hindered by its poor electrical conductivity (Liu *et al.*, 2024), short hole diffusion length (Yu *et al.*, 2018), and not negative enough conduction band position for efficient hydrogen evolution. The limitations cause a rapid recombination of the electrons and holes, resulting in a greatly reduced photoelectrochemical efficiency. Therefore, some modification strategies are needed to enhance charge separation and surface reaction kinetics. A good strategy is by the addition of secondary semiconductors that enhance charge transport and catalytic activity. Graphitic carbon nitride (g-C_3N_4) has been considered as a promising modifier due to its chemical stability, visible light absorption, low cost, and relatively negative conduction band position (Ahmed *et al.*, 2024), which provides a strong reductive driving force for efficient electron transfer in photoelectrochemical systems (Pei *et al.*, 2023; Wang *et al.*, 2021). It can be prepared from nitrogen-rich precursors such as urea, melamine and dicyandiamide. The structural and electronic properties of g-C_3N_4, including the band gap, flat band potential, and charge transport properties, are strongly influenced by the precursor type. Various precursors have been reported to generate different morphology (Xia *et al.*, 2022) and photocurrent densities, e.g. 162.3 μA/cm^2 (urea), 30 μA/cm^2 (melamine), and 63 μA/cm^2 (dicyandiamide) (Zhu *et al.*, 2022). The variations indicate the importance of precursor selection on the material performance.

Recently, it has been reported that the combination of multiple precursors can change the morphology and electronic structure of g-C_3N_4, which can affect the photocatalytic performance of g-C_3N_4 (Zhang *et al.*, 2019). The hybrid precursor systems have been reported to influence the porosity, surface area and electron transport properties that may affect the active site availability and charge carrier dynamics. Nevertheless, studies investigating hybrid precursor-derived g-C_3N_4 in α-Fe_2O_3/g-C_3N_4 PEC systems remain relatively limited. In this context, the coupling of α-Fe_2O_3 with g-C_3N_4 is a promising strategy to improve the photoanode performance. The introduction of g-C_3N_4 is expected to facilitate interfacial charge transfer through heterojunction formation (such as type-II or Z-scheme configurations) (Duan & Mei, 2020) rather than primarily improving visible-light absorption. Type-II heterojunctions may promote spatial separation of photogenerated charge carriers, while Z-scheme configurations can retain strong redox potentials during interfacial charge transfer. These interfacial charge transfer pathways are complementary to the intrinsic photoactivity of α-Fe_2O_3, resulting in improved photoelectrochemical performance. The combination of both materials may influence charge carrier separation behavior and the overall photoelectrochemical activity (Ong *et al.*, 2016). Therefore, α-Fe_2O_3/g-C_3N_4 heterostructures are a promising strategy for low-cost and efficient PEC systems. The synthesis of α-Fe_2O_3 and α-Fe_2O_3/g-C_3N_4 composites has been reported in several studies. α-Fe_2O_3 has been synthesized by hydrothermal method(Kawde *et al.*, 2021) and α-Fe_2O_3/g-C_3N_4 composites have been prepared by hydrothermal synthesis followed by impregnation with various g-C_3N_4 loadings from urea precursors. Moreover, oxidation of HMF in PEC systems has been investigated with different photoanodes and mediators (Kawde *et al.*, 2021; Lhermitte *et al.*, 2021). Despite these advancements, there has been limited research on α-Fe_2O_3/g-C_3N_4 systems with hybrid precursor-derived g-C_3N_4 for PEC applications, particularly for systems involving HMF-assisted processes. Thus, this study investigates the influence of hybrid precursor-derived g-C_3N_4 on the structural, optical, and photoelectrochemical properties of α-Fe_2O_3/g-C_3N_4 photoanodes under HMF-assisted PEC conditions.

2. Material and Method

2.1. Materials

Fluorine-doped tin oxide (FTO) glass substrates were employed as the conductive support. Urea ($CO(NH_2)_2$, 99.5%, Merck), melamine ($C_3H_6N_6$, 99%, Merck) and dicyandiamide ($C_2H_4N_4$, 99%, Merck) were used as precursors for the synthesis of g-C_3N_4. Iron(III) chloride ($FeCl_3$, 97%, Sigma-Aldrich) and sodium nitrate ($NaNO_3$, 99%, Merck) were used as precursors for α-Fe_2O_3 synthesis. Ethanol (C2H5OH, 99.9%, Merck) and acetone (C3H6O, technical) were used as cleaning solvents. Electrolyte was prepared using potassium chloride (KCl, Merck, 99%). All experimental procedures were performed with deionized (DI) water. The electrolyte contained 5-Hydroxymethylfurfural (HMF, C6H6O3, 99%, Sigma-Aldrich) as a model organic substrate. All chemicals were purchased from the respective suppliers and used without further purification.

2.2. Synthesis of α-Fe_2O_3 film

α-Fe_2O_3 thin films were deposited on fluorine-doped tin oxide (FTO) glass substrates by hydrothermal route. FTO substrates (10 mm × 50 mm) were cleaned with a mixture of ethanol and acetone (1:1, v/v) and rinsed with deionized (DI) water prior to synthesis. The precursor solution was prepared by dissolving 4.055 g of FeCl 3 and 8.50 g of NaNO 3 in 100 mL of DI water, with continuous stirring, until a homogeneous orange solution was obtained. Then, 60 mL of the prepared solution was transferred into a 100 mL Teflon-lined stainless-steel autoclave. The cleaned FTO substrate was then dipped in the solution with the conductive side down. The autoclave was sealed and kept at 195 °C for 6 h under its own pressure. After the reaction, the system was cooled to room temperature naturally. The obtained samples were removed, rinsed with acetone and dried in a nitrogen (N_2) stream. The substrates were washed with DI water and ultrasonicated for 5 min to remove loosely bound particles. Finally, the samples were dried for 2 h in an oven at 60 °C.

Table 1
Sample nomenclature and corresponding descriptions of α-Fe_2O_3 and α-Fe_2O_3/g-C_3N_4 photoanodes, along with g-C_3N_4 powders synthesized using single, binary, and ternary precursor combinations.

Sample Name	Description
Fe_2O_3	α-Fe_2O_3 photoanode without the addition of g-C_3N_4
Fe-U	α-Fe_2O_3/g-C_3N_4 photoanode with g-C_3N_4 prepared using urea precursor
Fe-D	α-Fe_2O_3/g-C_3N_4 photoanode with g-C_3N_4 prepared using dicyandiamide precursor
Fe-M	α-Fe_2O_3/g-C_3N_4 with g-C_3N_4 prepared using melamine precursor
Fe/U-D	α-Fe_2O_3/g-C_3N_4 with g-C_3N_4 prepared using urea:dicyandiamide precursor (1:1)
Fe/U-M	α-Fe_2O_3/g-C_3N_4 with g-C_3N_4 prepared using urea:melamine precursor (1:1)
Fe/M-D	α-Fe_2O_3/g-C_3N_4 with g-C_3N_4 prepared using melamine:dicyandiamide precursor (1:1)
Fe/U-M-D	α-Fe_2O_3/g-C_3N_4 with g-C_3N_4 prepared using urea:dicyandiamide:melamine precursor (1:1:1)
CN/U-D	g-C_3N_4 prepared using urea:dicyandiamide precursor ratio of 1:1
CN/U-M	g-C_3N_4 prepared using urea:melamine precursor ratio of 1:1
CN/M-D	g-C_3N_4 prepared using melamine:dicyandiamide precursor ratio of 1:1
CN/U-M-D	g-C_3N_4 prepared using urea:melamine:dicyandiamide precursor ratio of 1:1:1
CN/U	g-C_3N_4 prepared using urea precursor
CN/M	g-C_3N_4 prepared using melamine precursor
CN/D	g-C_3N_4 prepared using dicyandiamide precursor

2.3. g-C_3N4 coating on α-Fe_2O_3 for the synthesis of α-Fe_2O_3/g-C_3N_4 film

Thermal polymerization of urea, melamine and/or dicyandiamide precursors with different compositions was used to synthesize g-C_3N_4 powder. A total of 20 g of precursor mixtures with different ratios (0:0:0, 1:0:0, 0:1:0, 0:0:1, 1:1:0, 1:0:1, 0:1:1, and 1:1:1) were mixed thoroughly before calcination. The mixtures were heated at 550 °C for 5 h to obtain g-C_3N_4 powder, then ground to obtain a fine and homogeneous material. For preparation of g-C_3N_4 dispersion, 100 mg of the obtained powder was dispersed in 100 mL of isopropyl alcohol. The suspension was ultrasonicated for 12 h to help exfoliation and then centrifuged at 3000 rpm for 10 min. The supernatant was then collected to a volume of 30 mL for further processing. The α-Fe_2O_3 films were coated with g-C_3N_4 by means of an impregnation method. The films were soaked in the prepared g-C_3N_4 dispersion for 15 min followed by drying at 90 °C. This deposition-drying process was considered as one cycle and repeated 9 cycles for sufficient loading. The as-prepared α-Fe_2O_3 /g-C_3N_4 films were further calcined at 350 °C for 1 h and cooled down naturally to room temperature. The prepared α-Fe_2O_3/g-C_3N_4 photoanodes were then used for further characterization and photoelectrochemical analysis, where the active electrode area was limited to 0.5 cm × 0.5 cm during PEC measurements.

2.4. Sample Nomenclature

In order to have a clear and consistent sample identification, a systematic nomenclature based on the precursor composition used for the g-C_3N_4 synthesis was employed. Abbreviations: U, urea; M, melamine; D, dicyandiamide. The notation "Fe/" indicates the use of α-Fe_2O_3 as the base photoanode and the subsequent letters indicate the type and combination of precursors used to derive g-C_3N_4. Single, binary and ternary combination are indicated as such which allows for easy differentiation between samples. Table 1 gives a detailed description of all sample codes.

2.5. Characterization

The functional groups and bonding structures of the synthesized materials were studied by Fourier transform infrared (FTIR) spectroscopy using a Thermo Scientific Nicolet iS5 spectrometer. Spectra were taken in the 400-4000 cm^{-1} range with a DTGS KBr detector and KBr beamsplitter. All measurements were performed using 16 sample scans and 64 background scans to provide adequate signal quality. X-ray diffraction (XRD) analysis was performed to study the crystalline structure and phase composition of the samples by using a Rigaku Miniflex 600 diffractometer with Cu Kα radiation (λ = 1.5406 Å) and a 1D D/teX Ultra detector. The measurements were performed in the 2θ range from 10 to 80° at a scanning rate of 10° min^{-1}. The optical properties of the fabricated photoanodes were measured by UV–Vis diffuse reflectance spectroscopy (DRS) performed on an Agilent Cary 60 UV–Vis spectrophotometer in the range of 200–800 nm. The energy of the band gap was calculated from the DRS spectra by the Tauc relation (Eq. 1):

$$(\alpha h\nu)^n = A(h\nu - E_g) \quad (1)$$

where h is Planck's constant, v is the photon frequency, α is the absorption coefficient and A is a proportionality constant. The exponent n depends on the type of the electronic transition. Indirect transition (n=2) was used to calculate the band gap energy of the α-Fe_2O_3/g-C_3N_4 photoanodes, considering that the main phase in the composite (>90%) is α-Fe_2O_3. To investigate the recombination behavior of the photogenerated charge carriers, photoluminescence (PL) analysis of the thin film samples was carried out. The emission spectra were recorded on a Horiba MicOSPhotoluminescence, with an excitation wavelength of 325 nm and recording emission from 350 to 1100 nm.

2.6. Photoelectrochemical Measurement

Electrochemical measurements were performed in a typical three-electrode configuration with Pt mesh as the counter electrode, Ag/AgCl as the reference electrode, and α-Fe_2O_3 /g-C_3N_4 as the working electrode. The experiments were performed in electrolyte 1 M KCl under illumination of UV-visible light, with 30 W LED lamp as a source of light. The onset potential was determined from the LSV curves as the potential at which the photocurrent began to deviate noticeably from the baseline current. All potentials reported in this work were measured against an Ag/AgCl reference

3. Results and Discussion

3.1. Material Characterization

The functional groups and the bonding structure of the synthesized photoanodes were studied by FTIR spectroscopy

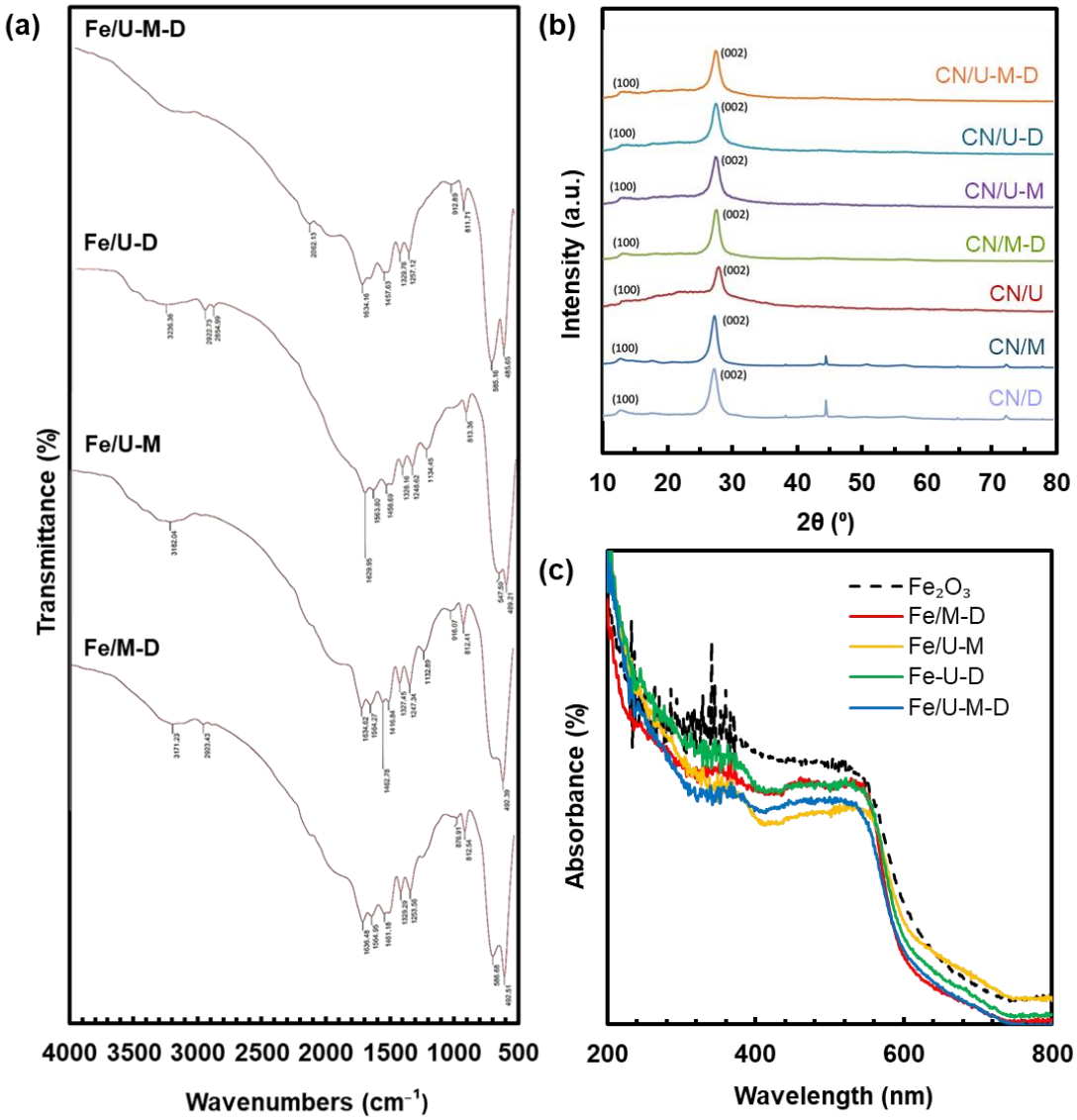

Fig 1. (a) FTIR spectra of α-Fe_2O_3/g-C_3N_4 (Fe/U–M–D) photoanodes; (b) XRD patterns of g-C_3N_4 synthesized from different hybrid precursor compositions; and (c) UV–vis spectra of α-Fe_2O_3/g-C_3N_4 photoanodes.

(Figure 1a). The α-Fe_2O_3 spectrum shows characteristic peaks at ~469 and 542 cm $^{-1}$ attributed to Fe–O stretching vibrations. For g-C_3N_4, two different regions are observed: bands in the range 1210–1640 cm^{-1} assigned to C–N and C=N stretching of the aromatic framework (Ma *et al.*, 2017) and a sharp peak at ~810 cm^{-1} assigned to the breathing mode of the heptazine units (Thaweesak *et al.*, 2017). The observed characteristic features in the composite samples (Fe/U-M, Fe/U-D, Fe/M-D, and Fe/U-M-D) indicate the presence of g-C_3N_4 within the α-Fe_2O_3-based composite films.

XRD patterns of g-C_3N_4 prepared with different compositions of hybrid precursors are shown in Figure 1b. The diffraction peaks at ~13.1° and 27.4° are attributed to the (100) and (002) planes of g-C_3N_4 (JCPDS No. 87-1526),(Zhao *et al.*, 2019) respectively, which are the evidence of in-plane structural ordering and interlayer stacking of the conjugated framework. The precursor composition has an effect on the crystallinity, where CN/M–D shows the highest peak intensity and higher degree of crystallinity than the urea-containing systems (CN/U–M, CN/U–D, and CN/U–M–D). This reduction in crystallinity is probably associated with gas evolution during the decomposition of urea, which may disturbs the structural ordering during condensation process (Dong *et al.*, 2018). The crystallite size analysis (Table 2) demonstrates that hybrid precursor systems produce smaller crystallite sizes (13.05–17.79 nm) than g-C_3N_4 obtained from single precursor, with samples containing urea having the smallest sizes, consistent with previous studies (Ibadurrohman *et al.*, 2024). The reduced crystallite size may influence the surface characteristics and charge transfer behavior of the material, which could contribute to the observed photoelectrochemical response.

The optical properties of the photoanodes were investigated using UV–vis diffuse reflectance spectroscopy (Figure 1c). The absorption edges of Fe_2O_3, Fe/M–D, Fe/U–M, Fe/U–D, and Fe/U–M–D were observed at 689, 639, 663, 654, and 642 nm, respectively. The incorporation of g-C_3N_4 results in a slight blue shift in the absorption edge, accompanied by a marginal increase in band gap energy to 1.93–2.03 eV. This trend is consistent with the wider band gap of g-C_3N_4 relative to α-Fe_2O_3, indicating electronic structure modulation upon

Table 2
g-C3N4 Crystal Size with Hybrid Precursors.

Sample	2θ	FWHM	L (nm)
CN/D	27.24	0.81	32.21
CN/M	27.31	0.61	48.86
CN/U	27.81	1.09	34.28
CN/M-D	27.52	1.207	17.79
CN/U-M	27.47	1.349	15.09
CN/U-D	27.46	1.334	15.12
CN/U-M-D	27.38	1.406	13.05

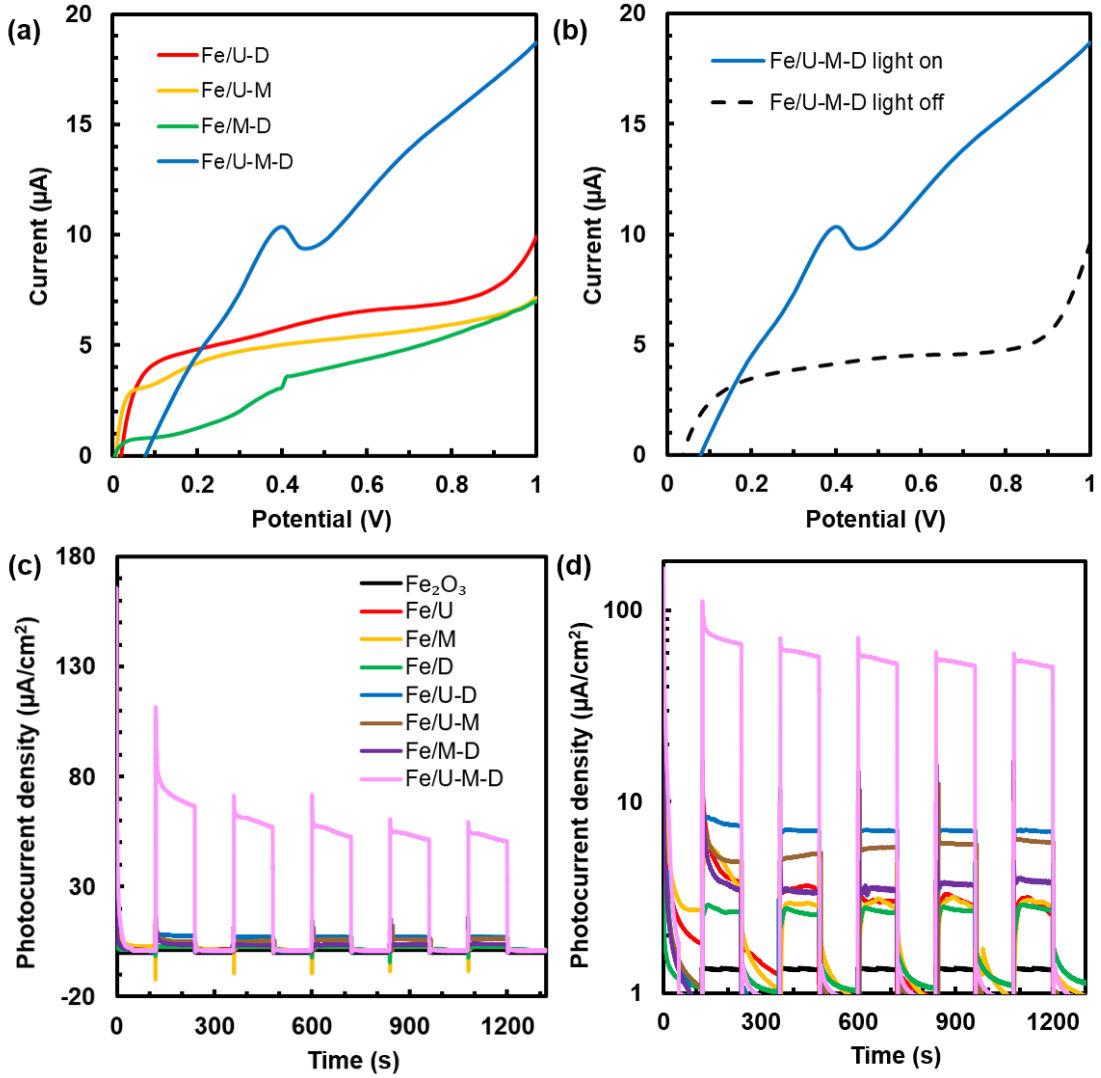

Figure 2. (a) Linear sweep voltammetry (LSV) curves of α-Fe_2O_3/g-C_3N_4 photoanodes with different hybrid precursor compositions under illumination (scan rate of 10 mV s^{-1}); (b) corresponding LSV curve of the best-performing sample (Fe/U–M–D); (c) chronoamperometry responses under intermittent light irradiation at 1.0 V (2 min dark–2 min light cycles, repeated five times); and (d) chronoamperometry data displayed on a logarithmic scale.

composite formation. Despite this shift, all samples remain active within the visible light region. More importantly, the incorporation of g-C_3N_4 may influence charge separation and interfacial charge transfer behavior through possible heterojunction interaction, which could contribute to the observed enhancement in photoelectrochemical performance.

3.2. Photo-electrochemical Characterization

Figure 2a presents the onset potentials of Fe/M–D, Fe/U–M, Fe/U–D, and Fe/U–M–D photoanodes under illumination, with comparison to dark conditions shown in Figure 2b. Under light irradiation, all photoanodes exhibit a noticeable shift in onset

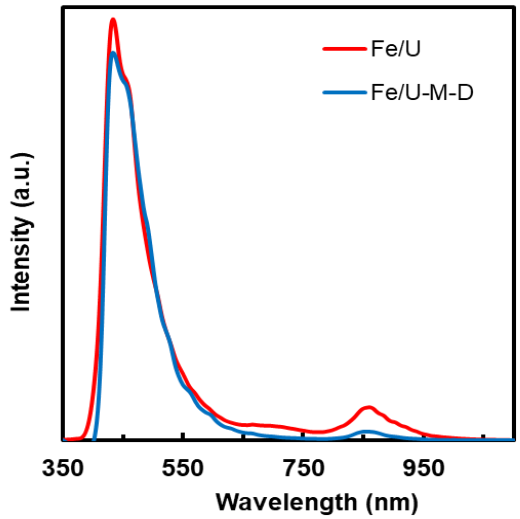

Fig 3. Photoluminescence (PL) spectra of α-Fe_2O_3/g-C_3N_4 photoanodes synthesized using single precursor (Fe/U) and hybrid precursor (Fe/U–M–D), recorded at an excitation wavelength of 325 nm, illustrating reduced emission intensity for the hybrid system, indicative of suppressed electron–hole recombination.

potential toward lower values, indicating reduced energy requirements to initiate the reaction. This behavior is attributed to the generation of electron–hole pairs upon light absorption, which assists the electrochemical process and decreases the need for external bias. The difference in onset potential (ΔE) reflects the relative shift in onset potential under illumination. The onset potentials for Light Off, Fe/M–D, Fe/U–M, Fe/U–D, and Fe/U–M–D were determined to be 0.89, 0.03, 0.03, 0.07, and 0.01 V, respectively, corresponding to ΔE values of 0.00, 0.86, 0.86, 0.82, and 0.88 V. Among all samples, Fe/U–M–D exhibited the lowest onset potential and the highest ΔE under the present experimental conditions, indicating improved photoelectrochemical response under the tested conditions. In addition, the photocurrent density under illumination is significantly higher than that under dark conditions, suggesting improved photoresponse under illumination.

The negligible current observed in the absence of light further emphasizes the critical role of photoactivation in driving the reaction, demonstrating the important role of photoactivation in driving the electrochemical response. Chronoamperometry measurements were performed with intermittent light irradiation (2 min dark–2 min light cycles, repeated five times), as shown in Figure 2(c-d). The data in Figure 2d are presented on a logarithmic scale to improve visualization, whereas the original linear-scale data are provided in Figure 2c. The photocurrent densities of all composite photoanodes (Fe/M-D, Fe/U-M, Fe/U-D, and Fe/U-M-D) were higher than that of the pristine α-Fe_2O_3, which suggests that the formation of α-Fe_2O_3/g-C_3N_4 heterojunctions could enhance charge separation and transport. FTIR analysis also confirmed the presence of g-C_3N_4 by characteristic C-N-C and C-N heterocyclic vibrations. Transient photocurrent responses show an initial sharp increase upon illumination, which can be explained by the rapid photogeneration of charge carriers, followed by a decay to a steady state value due to recombination processes. The rate of decay indicates the competition between charge generation and recombination (Mokhtarimehr & Tatarkova, 2017). In particular, Fe/U–M–D shows a more stable photocurrent response, suggesting the enhanced charge carrier dynamics. This conclusion is also supported by the photoluminescence analysis (Figure 3). The emission intensity of Fe/U–M–D is lower than that of Fe/U, indicating that the recombination of electron–hole pairs is suppressed and the charge separation is more effective, contributing to the improved photoelectrochemical performance.

3.3. Hybrid Precursor Effects

The improved photoelectrochemical activity of the samples prepared from hybrid precursors (urea, melamine, and dicyandiamide) shows a clear synergistic effect in the α-Fe_2O_3/g-C_3N_4 system. This behavior agrees with previous studies on thiourea derived g-C_3N_4, where hybrid precursor routes have been reported to favor the formation of mixed triazine- and heptazine-based structures (Jing *et al.*, 2020). From a structural point of view, heptazine units have a more extended π-conjugated system than triazine, which allows for the delocalization of more electrons and more efficient creation and transport of charge carriers. The relevance of this mechanism to the present system can be understood from the similarity in the thermal decomposition pathways of urea and thiourea. The two precursors in the calcination process give cyanamide intermediates that polymerize to g-C_3N_4 frameworks. Such similarity in the hybrid systems with urea indicates the ability to induce similar structural motifs, which lead to better electronic properties. The experimental results show this structural effect, with Fe/U-D and Fe/U-M having higher photoelectrochemical activity than Fe/M-D and Fe/U-M-D having the highest performance of all. The improved activity of Fe/U–M–D may be associated with the combined influence of the different precursors on the structural and electronic properties of g-C_3N_4.. Thus, the hybrid system has a smaller crystallite size (Table S1) which may influence the surface characteristics and charge transfer behavior of the material.

Meanwhile, the improved performance might be attributed to the interfacial charge transfer between α-Fe_2O_3 and g-C_3N_4 through heterojunction construction. The more positive conduction band position of α-Fe_2O_3 is less favorable for proton reduction, whereas g-C_3N_4 possesses a more negative conduction band potential and is thermodynamically more suitable for reduction reactions. Under illumination, the photogenerated charge carriers may be spatially separated across the heterojunction interface, which may result in suppressed charge recombination and improved photoelectrochemical response. This type of interfacial charge transfer may follow type-II or Z-scheme heterojunction behavior, as reported in previous studies (Lathe & palve, 2026). However, further band structure and charge transfer analyses are required to confirm the exact mechanism in the present system.

3.4. HMF-Assisted PEC Performance

In photoelectrochemical systems, the photoanodic reaction is typically limited by the oxygen evolution reaction (OER) that is energetically expensive and kinetically sluggish, but produces a low-value product (Luo *et al.*, 2021). To overcome this limitation, alternative oxidation pathways are often introduced using sacrificial agents that allow a more efficient hole consumption. Among these, the oxidation of 5-hydroxymethylfurfural (HMF) has been identified as a

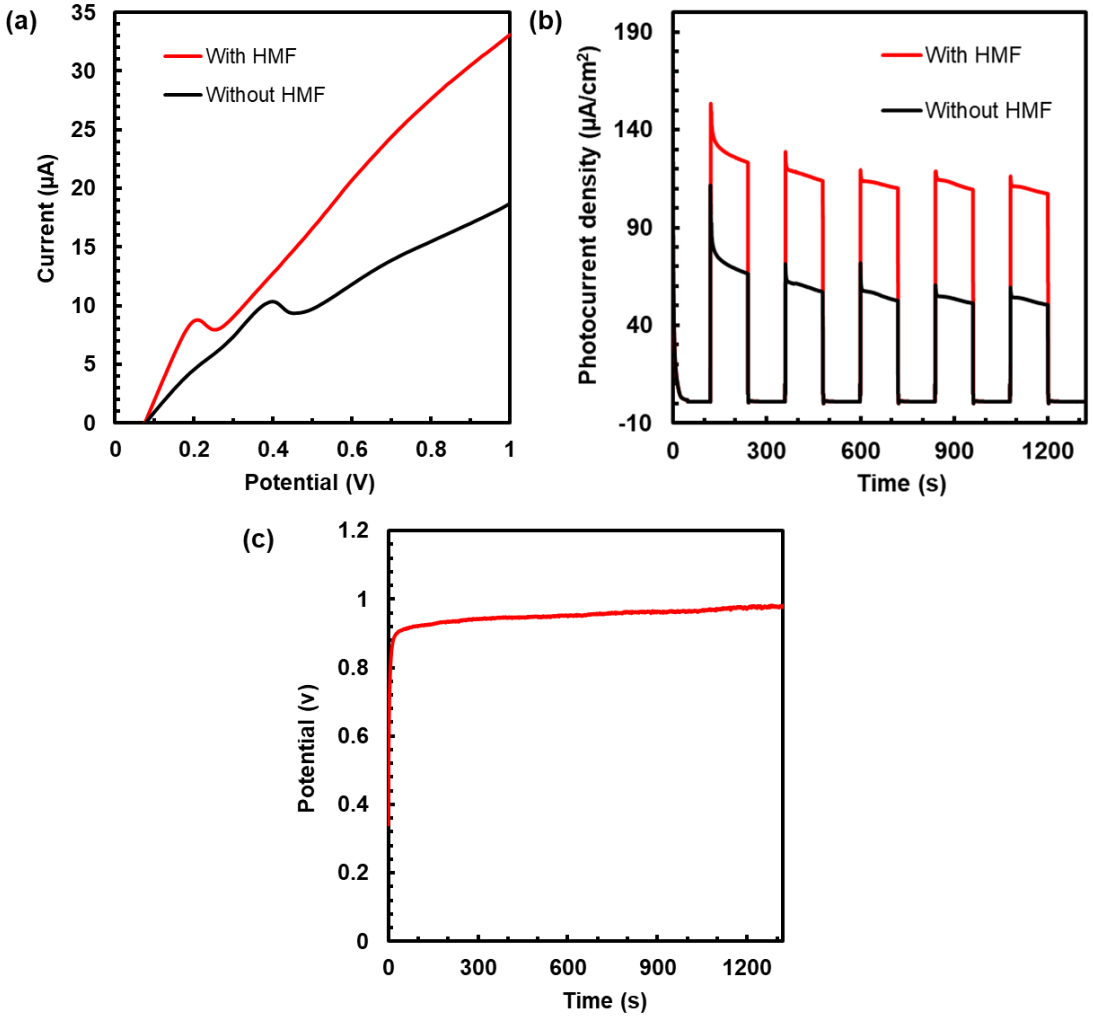

Fig 4. (a) Linear sweep voltammetry (LSV) and (b) chronoamperometry curves of Fe/U-M-D photoanodes with and without 10 mM HMF under illumination at 1.0 V; (c) Stability test using chronopotentiometry of Fe/U-M-D with 10 mM HMF at 30μA

promising alternative due to its faster kinetics and lower energy demand over OER. HMF was added to the electrolyte at a concentration of 10 mM in this study. The best performing photoanode, Fe/U–M–D, was then subjected to chronoamperometry measurements under the same cycling protocol (five cycles) to investigate the effect of HMF on the photoelectrochemical response.

LSV results show that the onset potential and ΔE are not affected by the inclusion of HMF in the electrolyte. As presented in Figure 4a, Fe/U–M–D and Fe/U–M–D with HMF have the same onset potential of 0.01 V and ΔE value of 0.88 V. However, a great increase in the current density is observed in the whole potential range in the presence of HMF. The enhanced current response indicates better charge carrier utilization where HMF acts as an efficient hole scavenger that results in faster consumption of holes and suppression of recombination. This behavior is in accordance with the chronoamperometry results, suggesting that the existence of HMF facilitates the photocurrent generation and improves the overall photoelectrochemical performance.

The photocurrent density of the Fe/U–M–D photoanode with and without 10 mM HMF at 1.0 V was 59.98 and 116.97 μA cm^{-2}, respectively (Figure 4b). The presence of HMF led to a significant increase in photocurrent density of approximately 95%, indicating improved hole consumption during the photoelectrochemical process. This behavior is associated with the role of HMF as a hole-accepting species that can compete with the oxygen evolution reaction and reduce charge carrier recombination. Chronopo-tentiometric measurements were conducted under continuous illumination for 2 h 40 min to evaluate the photo-response under continuous operation. Figure 4c shows that the measurement was performed at a constant current of 30 μA, which was selected based on the photocurrent response observed from the LSV curve of the Fe/U–M–D photoanode in the presence of HMF. The potential rapidly stabilized and remained close to ~1 V throughout the measurement period, indicating relatively stable electrochemical behavior under the tested conditions. This potential response is consistent with the LSV results, where a photocurrent of ~30 μA was obtained at ~1 V. Minor potential fluctuations were still observed during the measurement and may be attributed to interfacial charge transfer processes during continuous PEC operation.

4. Conclusion

α-Fe_2O_3/g-C_3N_4 photoanodes were successfully fabricated using g-C_3N_4 derived from ternary hybrid precursors (urea–melamine–dicyandiamide). Hybrid precursor engineering

influenced the crystallite size (13.05–17.79 nm) and optical properties, with absorption edges observed at 642–663 nm and band gap energies of 1.93–2.03 eV. Fe/U–M–D showed the best performance among all samples with an onset potential of 0.01 V, ΔE of 0.88 V and photocurrent density of 59.98 μA cm^{-2}. The addition of 10 mM HMF enhanced the photocurrent to 116.97 μA cm^{-2} (~95% increase) without any change in onset potential, indicating its role as an effective hole scavenger under the tested conditions. Chrono-potentiometric measurements also showed stable photoresponse behavior during 2 h 40 min of continuous operation at ~1 V and 30 μA. Overall, these findings demonstrate that hybrid precursor-derived g-C_3N_4 can influence the photoelectrochemical behavior of α-Fe_2O_3/g-C_3N_4 photoanodes under HMF-assisted PEC conditions.

Acknowledgement

The research reported in this paper is also partially supported by Seed Funding Hibah Lektor Kepala Skema Hibah Riset according to contract number NKB-3412/UN2.F4.D/PPM.00.00/2024

Reference

Ahmed, M. A., Mahmoud, S. A., & Mohamed, A. A. (2024). Unveiling the photocatalytic potential of graphitic carbon nitride (g-C3N4): a state-of-the-art review. *RSC Advances, 14*(35), 25629-25662. https://doi.org/10.1039/D4RA04234D

Al Dhahri, H., Hussain, M., Ghani, M. A. A., Inayat, A., Al-Muhtaseb, A. a. H., Al-Haj, L., & Jamil, F. (2026). Green hydrogen production via electrolysis: Materials innovation, system integration, and global deployment pathways. *Renewable and Sustainable Energy Reviews, 229*, 116617. https://doi.org/10.1016/j.rser.2025.116617

AlZohbi, G. (2025). Ammonia from Hydrogen: A Viable Pathway to Sustainable Transportation? *Sustainability, 17*(18), 8172. https://doi.org/10.3390/su17188172

Arabi, N., Babaei, S., Qi, J., Arvelli, S., & Zhao, J. (2026). A review of 5-hydroxymethylfurfural production from fructose using heterogeneous catalysts. *Biomass Futures, 1*, 100009. https://doi.org/10.1016/j.bmf.2025.100009

Ayed, C., Huang, W., Kizilsavas, G., Landfester, K., & Zhang, K. A. I. (2020). Photocatalytic Partial Oxidation of 5-Hydroxymethylfurfural (HMF) to 2,5-Diformylfuran (DFF) Over a Covalent Triazine Framework in Water. *ChemPhotoChem, 4*(8), 571-576. https://doi.org/10.1002/cptc.202000070

Bzovsky, I., & Kudriavtsev, S. (2025). Green hydrogen for sustainable ammonia production: PEM electrolysis powered by wind energy. *IOP Conference Series Earth and Environmental Science, 1491*. https://doi.org/10.1088/1755-1315/1491/1/012037

Chiang, C.-Y., Chang, M.-H., Liu, H.-S., Tai, C. Y., & Ehrman, S. (2012). Process Intensification in the Production of Photocatalysts for Solar Hydrogen Generation. *Industrial & Engineering Chemistry Research, 51*(14), 5207-5215. https://doi.org/10.1021/ie202522g

Corbin, J., Jones, M., Lyu, C., Loh, A., Zhang, Z., Zhu, Y., & Li, X. (2024). Challenges and progress in oxygen evolution reaction catalyst development for seawater electrolysis for hydrogen production. *RSC Advances, 14*(9), 6416-6442. https://doi.org/10.1039/d3ra08648h

Dong, H., Guo, X., Yang, C., & Ouyang, Z. (2018). Synthesis of g-C3N4 by different precursors under burning explosion effect and its photocatalytic degradation for tylosin. *Applied Catalysis B: Environmental, 230*, 65-76. https://doi.org/10.1016/j.apcatb.2018.02.044

Duan, B., & Mei, L. (2020). A Z-scheme Fe2O3/g-C3N4 heterojunction for carbon dioxide to hydrocarbon fuel under visible illuminance. *Journal of Colloid and Interface Science, 575*, 265-273. https://doi.org/10.1016/j.jcis.2020.04.112

Dubbink, G. H. C., Geverink, T. R. J., Haar, B., Koets, H. W., Kumar, A., van den Berg, H., van der Ham, A. G. J., & Lange, J.-P. (2021). Furfural to FDCA: systematic process design and techno-economic evaluation. *Biofuels, Bioproducts and Biorefining, 15*(4), 1021-1030. https://doi.org/10.1002/bbb.2204

Dumančić, A., Vlahinić, N., & Skok, M. (2024). Replacing Gray Hydrogen with Renewable Hydrogen at the Consumption Location Using the Example of the Existing Fertilizer Plant. *Sustainability, 16*(15), 6437. https://doi.org/10.3390/su16156437

Hossain Bhuiyan, M. M., & Siddique, Z. (2025). Hydrogen as an alternative fuel: A comprehensive review of challenges and opportunities in production, storage, and transportation. *International Journal of Hydrogen Energy, 102*, 1026-1044. https://doi.org/10.1016/j.ijhydene.2025.01.033

Hren, D. T., Bogataj, M., & Nemet, A. (2024). Methanol Production via Power-to-Liquids: A Comparative Simulation of Two Pathways Using Green Hydrogen and Captured CO2. *Processes, 12*(12), 2843. https://doi.org/10.3390/pr12122843

Hren, R., Vujanović, A., Van Fan, Y., Klemeš, J. J., Krajnc, D., & Čuček, L. (2023). Hydrogen production, storage and transport for renewable energy and chemicals: An environmental footprint assessment. *Renewable and Sustainable Energy Reviews, 173*, 113113. https://doi.org/10.1016/j.rser.2022.113113

Ibadurrohman, M., Ainin, A. Q., Alam, F. Z., Mumtazah, N., Slamet, Ferdiansyah Madsuha, A., Ulum, R. M., & Hasiholan, B. (2024). Modification of hydrothermally synthesized α-Fe2O3 nanorods with g-C3N4 prepared from various precursors as photoanodes for hydrogen production. *New Journal of Chemistry, 48*(33), 14746-14756. https://doi.org/10.1039/D3NJ05421G

Jing, H., You, M., Yi, S., Li, T., Ji, H., Wang, Y., Zhang, Z., Zhang, R., Chen, D., & Yang, H. (2020). Precursor-Engineering Coupled Microwave Molten-Salt Strategy Enhances Photocatalytic Hydrogen Evolution Performance of g-C3N4 Nanostructures. *ChemSusChem, 13*(4), 827-837. https://doi.org/10.1002/cssc.201902730

Kamat, P. V., & Sivula, K. (2022). Photoelectrochemical and Photocatalytic Hydrogen Generation: A Virtual Issue. *ACS Energy Letters, 7*(12), 4379-4380. https://doi.org/10.1021/acsenergylett.2c02492

Kawde, A., Sayed, M., Shi, Q., Uhlig, J., Pullerits, T., & Hatti-Kaul, R. (2021). Photoelectrochemical Oxidation in Ambient Conditions Using Earth-Abundant Hematite Anode: A Green Route for the Synthesis of Biobased Polymer Building Blocks. *Catalysts, 11*(8), 969. https://doi.org/10.3390/catal11080969

Lathe, A., & palve, A. M. (2026). A review on Type-I, Type-II, Z and S-scheme mechanisms involved in photocatalysis of inorganic and organic pollutant. *Next Materials, 11*, 101914. https://doi.org/https://doi.org/10.1016/j.nxmate.2026.101914

Lhermitte, C. R., Plainpan, N., Canjura, P., Boudoire, F., & Sivula, K. (2021). Direct photoelectrochemical oxidation of hydroxymethylfurfural on tungsten trioxide photoanodes. *RSC Advances, 11*(1), 198-202. https://doi.org/10.1039/D0RA09989A

Liu, B., Xu, S., Zhang, M., Li, X., Decarolis, D., Liu, Y., Wang, Y., Gibson, E. K., Catlow, C. R. A., & Yan, K. (2021). Electrochemical upgrading of biomass-derived 5-hydroxymethylfurfural and furfural over oxygen vacancy-rich NiCoMn-layered double hydroxides nanosheets. *Green Chemistry, 23*(11), 4034-4043. https://doi.org/10.1039/D1GC00901J

Liu, Y., Li, K., Dong, J., Xu, L., Li, Y., Wang, N., Li, S., & Ma, R. (2024). Enhancement of Stability and Conductivity of α-Fe2O3 Anodes by Doping with Cs+ for Lithium-Ion Battery. *ACS Applied Energy Materials, 7*(21), 9953-9961. https://doi.org/10.1021/acsaem.4c02038

Luo, H., Barrio, J., Sunny, N., Li, A., Steier, L., Shah, N., Stephens, I. E. L., & Titirici, M.-M. (2021). Progress and Perspectives in Photo- and Electrochemical-Oxidation of Biomass for Sustainable Chemicals and Hydrogen Production. *Advanced Energy Materials, 11*(43), 2101180. https://doi.org/10.1002/aenm.202101180

Ma, L., Fan, H., Fu, K., Lei, S., Hu, Q., Huang, H., & He, G. (2017). Protonation of Graphitic Carbon Nitride (g-C3N4) for an Electrostatically Self-Assembling Carbon@g-C3N4 Core–Shell Nanostructure toward High Hydrogen Evolution. *ACS Sustainable Chemistry & Engineering, 5*(8), 7093-7103. https://doi.org/10.1021/acssuschemeng.7b01312

Mokhtarimehr, M., & Tatarkova, S. A. (2017). Photocurrent transients of thin-film solar cells. *Journal of the Optical Society of America B, 34*(8), 1705-1712. https://doi.org/10.1364/JOSAB.34.001705

Møller, K. T., Jensen, T. R., Akiba, E., & Li, H.-w. (2017). Hydrogen - A sustainable energy carrier. *Progress in Natural Science: Materials International, 27*(1), 34-40. https://doi.org/10.1016/j.pnsc.2016.12.014

Mumtazah, N., Syahlani, N., Ibadurrohman, M., & Nasikin, M. (2026). H2O2-Driven Structural and Electronic Modulation of NiMn Electrocatalysts for Enhanced Electrooxidation of HMF to DFF. *ACS Omega*. https://doi.org/10.1021/acsomega.6c00066

Ong, W.-J., Tan, L.-L., Ng, Y. H., Yong, S.-T., & Chai, S.-P. (2016). Graphitic Carbon Nitride (g-C3N4)-Based Photocatalysts for Artificial Photosynthesis and Environmental Remediation: Are We a Step Closer To Achieving Sustainability? *Chemical Reviews, 116*(12), 7159-7329. https://doi.org/10.1021/acs.chemrev.6b00075

Pei, J., Li, H., Zhuang, S., Zhang, D., & Yu, D. (2023). Recent Advances in g-C3N4 Photocatalysts: A Review of Reaction Parameters, Structure Design and Exfoliation Methods. *Catalysts, 13*(11), 1402. https://doi.org/10.3390/catal13111402

Szablowski, L., Wojcik, M., & Dybinski, O. (2025). Review of steam methane reforming as a method of hydrogen production. *Energy, 316*, 134540. https://doi.org/10.1016/j.energy.2025.134540

Thaweesak, S., Wang, S., Lyu, M., Xiao, M., Peerakiatkhajohn, P., & Wang, L. (2017). Boron-doped graphitic carbon nitride nanosheets for enhanced visible light photocatalytic water splitting. *Dalton Transactions, 46*(32), 10714-10720. https://doi.org/10.1039/C7DT00933J

van de Krol, R. (2012). Principles of Photoelectrochemical Cells. In R. van de Krol & M. Grätzel (Eds.), *Photoelectrochemical Hydrogen Production* (pp. 13-67). Springer US. https://doi.org/10.1007/978-1-4614-1380-6_2

Wang, S., Zhang, J., Li, B., Sun, H., & Wang, S. (2021). Engineered Graphitic Carbon Nitride-Based Photocatalysts for Visible-Light-Driven Water Splitting: A Review. *Energy & Fuels, 35*(8), 6504-6526. https://doi.org/10.1021/acs.energyfuels.1c00503

Xia, P., Li, G., Li, X., Yuan, S., Wang, K., Huang, D., Ji, Y., Dong, Y., Wu, X., Zhu, L., He, W., & Qiao, L. (2022). Synthesis of g-C3N4 from Various Precursors for Photocatalytic H2 Evolution under the Visible Light. *Crystals, 12*(12), 1719. https://doi.org/10.3390/cryst12121719

Yu, L., Zhang, Y., He, J., Zhu, H., Zhou, X., Li, M., Yang, Q., & Xu, F. (2018). Enhanced photoelectrochemical properties of α-Fe2O3 nanoarrays for water splitting. *Journal of Alloys and Compounds, 753*, 601-606. https://doi.org/10.1016/j.jallcom.2018.04.258

Zeng, J., Li, J., Zhong, J., Yang, H., Lu, Y., & Wang, G. (2015). Improved Sun light photocatalytic activity of α-Fe2O3 prepared with the assistance of CTAB. *Materials Letters, 160*, 526-528. https://doi.org/10.1016/j.matlet.2015.08.037

Zhang, C., Liu, J., Huang, X., Chen, D., & Xu, S. (2019). Multistage Polymerization Design for g-C3N4 Nanosheets with Enhanced Photocatalytic Activity by Modifying the Polymerization Process of Melamine. *ACS Omega, 4*(17), 17148-17159. https://doi.org/10.1021/acsomega.9b01510

Zhang, T., Wei, H., Xiao, H., Li, W., Jin, Y., Wei, W., & Wu, S. (2020). Advance in constructing acid catalyst-solvent combinations for efficient transformation of glucose into 5-Hydroxymethylfurfural. *Molecular Catalysis, 498*, 111254. https://doi.org/10.1016/j.mcat.2020.111254

Zhao, X., Pan, D., Chen, X., Li, R., Jiang, T., Wang, W., Li, G., & Leung, D. Y. C. (2019). g-C3N4 photoanode for photoelectrocatalytic synergistic pollutant degradation and hydrogen evolution. *Applied Surface Science, 467-468*, 658-665. https://doi.org/10.1016/j.apsusc.2018.10.090

Zhu, X., Wang, Z., Zhong, K., Li, Q., Ding, P., Feng, Z., Yang, J., Du, Y., Song, Y., Hua, Y., Yuan, J., She, Y., Li, H., & Xu, H. (2022). Mo-O-Bi Bonds as interfacial electron transport bridges to fuel CO2 photoreduction via in-situ reconstruction of black Bi2MoO6/BiO2-x heterojunction. *Chemical Engineering Journal, 429*, 132204. https://doi.org/10.1016/j.cej.2021.132204

Zhu, Y., He, L., Ni, Y., Li, G., Li, D., Lin, W., Wang, Q., Li, L., & Yang, H. (2022). Recent Progress on Photoelectrochemical Water Splitting of Graphitic Carbon Nitride (g−CN) Electrodes. *Nanomaterials, 12*(14), 2374. https://doi.org/10.3390/nano12142374